

Date of publication February 30, 2026, date of current version May 3, 2025.

Digital Object Identifier 10.1109/ACCESS.2024.0429000

Efficient Power Transfer to Implanted Antennas

VARVARA MOUZI¹, NEKTARIOS MORAITIS¹, (Senior Member, IEEE), CONSTANTINE KAKOYIANNIS², (Member, IEEE), KONSTANTINA S. NIKITA¹, (Fellow, IEEE), and CONSTANTINOS VALAGIANNPOULOS¹, (Senior Member, IEEE)

¹School of Electrical and Computer Engineering, National Technical University of Athens, Athens GR-15780, Greece.

²Department of Antennas and Electromagnetic Modeling, IMST GmbH, Kamp-Lintfort DE-47475, Germany.

Corresponding author: C. Valagiannopoulos (e-mail: valagiannopoulos@ece.ntua.gr).

ABSTRACT Wireless power transfer between an external electromagnetic (EM) source and implanted dipoles into human body can be greatly assisted by employing a matching part atop of the skin. Two different approaches are proposed: one incorporating lossless layers that minimize the reflections and another dealing with active metasurfaces that boost the transmissivity. Obviously, the performance is higher in the latter scenario since gain media are involved; however, even with passive layers, significant enhancement in the coupling between the two radiators is achieved. These coupling scores exhibit substantial robustness under the condition of misaligned dipoles, a feature that renders them suitable to operate under experimental imperfections. The proposed concept has been experimentally demonstrated at bluetooth frequencies leading to strong enhancement of power transmission, even when the radiation patterns of the two antennas are heavily misaligned. Accordingly, the reported designs can be utilized in biomedical setups that call for fast and reliable wireless communication: from healthcare monitoring and biosensing to real-time drug delivery and bioimaging.

INDEX TERMS Biomedical communication, Electromagnetic coupling, Implants, Metasurfaces, Wireless power transfer.

I. INTRODUCTION

Implantable antennas have recently become very popular since they constitute an indispensable part of most modern biometric telemetry systems permitting the transmission of physiological signals at positions in and out of the human body [1]. Therefore, several research efforts are addressing the challenging aspects in the operation of implantable devices such as biocompatibility, miniaturization, patient safety, connectivity with exterior monitoring or control equipment, and insensitivity to detuning [2]. Importantly, several solutions regarding numerical simulations, designs and employed media have been proposed to tackle the weaknesses related to low data rate, restricted communication ranges, performance sensitivity to the positioning of various structural parts and limitations of invasive endoscopy [3].

In particular, dual-band implantable antennas are utilized for continuous glucose monitoring [4], folded slot dipoles are safely functioning across the medical band [5] while radiators into the skin can provide wireless measurements for pressure and temperature [6]. Moreover, miniature antennas for integration in head-implanted medical devices have been successfully introduced [7]; on the other hand, adding a parasitic patch over the human body has been proposed to

enhance the wireless power link between embedded rectennas and the exterior [8]. Finally, on-body repeaters are found to support wideband transmission [9], capacitively loaded circularly polarized implanted patches contribute positively to the link budget [10] and a similar device provides reliable subcutaneous real-time blood measurements [11].

Matching between one electromagnetic (EM) radiator that plays the role of transmitter and another receiving is one of the oldest topics in the scientific domain of wireless links since it is able to increase the signal-to-noise ratio at the receiver without using higher power at the primary source. Indicative examples contain from the deposition of graphene nanoribbons to enhance the coupling between optical antennas for enhanced photocarrier collection [12] and the usage of matching circuits in multiple-input, multiple-output radio frequency arrays [13] to the installation of passive superstrates that increase the microwave detectability of buried objects [14]. The same aim is well-served by zinc oxide antireflection coatings in solar cells [15] or silicon nanocones that minimize the EM reflection [16]. On the other hand, wireless power transfer achieved via resonating coils [17] or rectifier circuits [18] is also a form of maximal coupling that have extensive

biomedical applications involving magnetic resonance imaging [19] and implantable sensing [20].

With the advent of electromagnetic metasurfaces, with which the fundamental laws of reflection and refraction were reformulated and arbitrarily exotic boundary conditions got feasible [21], the impedance matching became just a special case of the broad aim for generic controlling propagation and coupling of modes [22]. More specifically, metamaterial covers can flexibly tailor the receiving patterns of antennas with great benefits in the design and optimization of near-field sensors [23] while bilayer plasmonic metasurfaces can efficiently manipulate the visible light [24] and block interferences [25]. Importantly, metasurfaces may employ phase-change active materials giving tunable optical transmission [26] or nonlinear elements that enable efficient wavelength mixing with relaxed phase-matching conditions, ideal for realizing broadband frequency conversions and phase conjugation [27]. In addition, strong interference in ultra-thin films has been proposed as an effective mechanism for optimal absorption [28] while closed metasurfaces can leverage the EM radiation from multiple sources leading to green and secure communications [29]. Finally, metasurfaces can be engineered to control EM fields around and into the human body [30] and build novel optical biosensors [31] by overcoming the current limitations [32] of bioelectronic interfaces.

In this work, which is based on the thesis [33], we examine the external dipole coupling with implantable antennas to treat a simple and frequently met problem comprising one primary radiator into free space and another secondary receiver embedded into human tissue. Since specific levels of penetrating power is a prerequisite for any biosensor to operate efficiently, re-transmit securely the signals and record reliably the responses, maximal coupling between the two antennas is vital. Two ways of matching free space with the human body are proposed: one by depositing dielectric layers and another by utilizing EM metasurfaces. Approximate mathematical models are employed and the optimal setups are determined with use of Fabry-Perot resonant cavities in the former scenario and by assuming active structures with gain media in the latter one. Extensive numerical simulations with help from commercial software packages are executed, where theoretical predictions are validated; particular emphasis is given on the case of misaligned dipoles, where the robustness of the matching components is demonstrated. Importantly, we have experimentally measured significant wideband boost in the transmission through a suitably designed ceramic layer, even when the emitter is not optimally oriented with respect to the receiver. The reported results may assist substantially the modeling and design of medical instruments with a wide range of applications from healthcare monitoring and screening to bioelectromagnetic imaging and diagnostics.

II. MATHEMATICAL MODELING

We consider a system of two antennas: the first one radiates into free space and provides the primary excitation at bluetooth wavelengths while the second one is buried into the

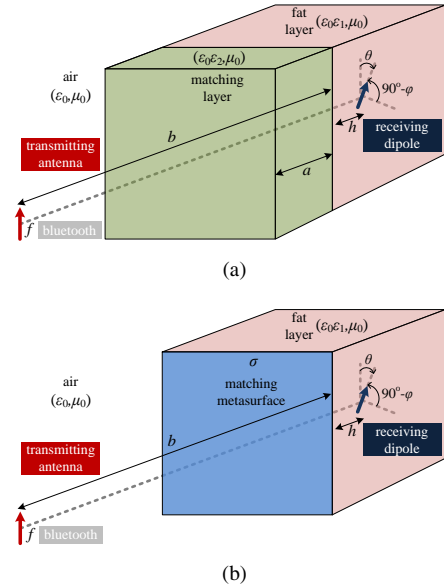


FIGURE 1. The physical configuration of the examined setups. A transmitting dipole antenna working at bluetooth frequency illuminates human tissue located at distance b , into which another dipole tilted by angles (θ, φ) has been placed. To enhance the penetration of the EM signal into the layer of human fat we utilize: (a) a matching layer of thickness $a < b$ and relative permittivity ϵ_2 and (b) a matching metasurface of complex surface conductivity σ . The complex relative permittivity of the human tissue is denoted by ϵ_1 .

human tissue. The first dipole is placed at distance b from the air-fat interface and the second dipole at distance h from it, as shown in Fig. 1. In order to maximize the coupling between the two antennas so that all the related diagnostic, monitoring and sensing applications are better facilitated, we propose the use either of a dielectric layer of thickness $a < b$ and relative complex permittivity ϵ_2 (depicted in Fig. 1(a)) or a metasurface of complex surface conductivity σ (depicted in Fig. 1(b)). Since the orientation of the receiving passive dipole may change into the body of the patient, we permit it to be misaligned with respect to the axis of the external source by angle θ and rotated by angle φ while being parallel to the boundary between the two media.

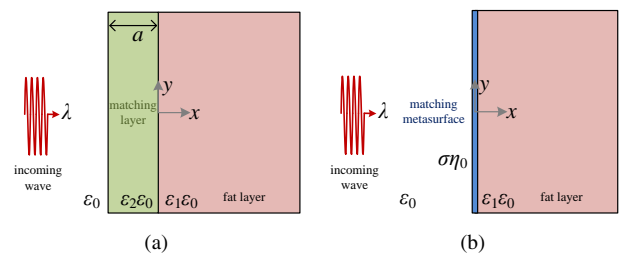


FIGURE 2. Simplistic one-dimensional models for the two scenarios of Fig. 1. The receiving dipoles have been conditionally removed while the transmitted antennas have been replaced by normally incident waves of wavelength λ .

In order to understand better the conditions that lead to maximal coupling between the two dipoles, we introduce two

one-dimensional analytically solvable models, one for each of the configurations of Fig. 1. The actual structures of Fig. 1 can be also treated in a rigorous manner which involves integral equations [34], [35] where the field quantities are approximated by finite sums of basis functions; however, in such a case, the final formulas are not easily physically interpretable. In Fig. 2(a), we consider as excitation into free space a normally incident plane wave of the same bluetooth oscillating wavelength $\lambda \cong 122.5$ mm. If one ignores the receiving dipole, the reflection coefficient reads:

$$R_L = e^{2ik_0a} \times \frac{e^{ik_2a}(k_0 - k_2)(k_1 + k_2) - e^{-ik_2a}(k_1 - k_2)(k_0 + k_2)}{e^{ik_2a}(k_0 - k_2)(k_1 + k_2) - e^{-ik_2a}(k_1 - k_2)(k_0 - k_2)}, \quad (1)$$

where $k_0 = 2\pi/\lambda$ is the wavenumber into air and $k_1 = k_0\sqrt{\varepsilon_1}$, $k_2 = k_0\sqrt{\varepsilon_2}$, the wavenumbers into fat and matching layer respectively.

By calling for perfect matching so that maximal power enters the area of the receiver (given the fact that the losses of the mediator slab are negligible), we derive the condition from (1):

$$R_L = 0 \Rightarrow e^{4\pi i\sqrt{\varepsilon_2}a/\lambda} = \frac{(1 + \sqrt{\varepsilon_2})(\sqrt{\varepsilon_1} - \sqrt{\varepsilon_2})}{(1 - \sqrt{\varepsilon_2})(\sqrt{\varepsilon_1} + \sqrt{\varepsilon_2})}. \quad (2)$$

If we assume that, apart from the intermediate layer, the fat half-space is also lossless and non-plasmonic ($\varepsilon_2 > 1$), the right-hand side of (2) is a real number. That forces the left-hand side of (2) to take specific values (± 1); however, the equation $e^{4\pi i\sqrt{\varepsilon_2}a/\lambda} = 1$ leads to the solution $\varepsilon_2 = 0$, which is rejected. Therefore, the perfect matching conditions are written as:

$$\left\{ \frac{a}{\lambda} \cong \frac{2m+1}{4\sqrt{\varepsilon_2}}, m \in \mathbb{N} \text{ and } \varepsilon_2 \cong \sqrt{\varepsilon_1} \right\}. \quad (3)$$

The equalities are approximate since ε_1 , in practice, is a complex number.

In Fig. 2(b), we sketch the respective one-dimensional model, once the matching metasurface of complex surface conductivity σ is used. The boundary conditions between air with EM fields (\mathbf{E} , \mathbf{H}) and fat with EM fields (\mathbf{E}_1 , \mathbf{H}_1) are given by [36]:

$$\hat{\mathbf{n}} \times (\mathbf{E}_1 - \mathbf{E})|_{x=0} = \mathbf{0},$$

$$\hat{\mathbf{n}} \times (\mathbf{H}_1 - \mathbf{H})|_{x=0} = -\sigma \hat{\mathbf{n}} \times (\hat{\mathbf{n}} \times \mathbf{E})|_{x=0},$$

where $\hat{\mathbf{n}} = \hat{\mathbf{x}}$ is the unitary vector normal to the air/fat interface ($x = 0$), as defined in Fig. 2(b). By imposing them, we analytically derive the reflection coefficient:

$$R_M = \frac{1 - \sqrt{\varepsilon_1} - \sigma\eta_0}{1 + \sqrt{\varepsilon_1} + \sigma\eta_0}. \quad (4)$$

Apparently, the perfect matching condition reads from (4):

$$R_M = 0 \Rightarrow \sigma = \frac{1 - \sqrt{\varepsilon_1}}{\eta_0}. \quad (5)$$

III. NUMERICAL RESULTS AND SIMULATIONS

A. EXTERNAL/INTERNAL DIPOLES MISMATCH

To illustrate more clearly the issue of poor coupling between the external EM antennas and the implanted dipoles, we may consider the configurations of Fig. 1 without the matching mediator between air and the human skin. In real-world operation, the transmitter radiates at bluetooth frequency $f \cong 2.45$ GHz, where the complex dielectric constant of human fat equals to: $\varepsilon_1 \cong 5.28(1 - 0.14i)$ [37]–[39]. In Fig. 3, we regard the initial system without any additional matching equipment and test the behavior of the two antennas in the spectral vicinity of bluetooth frequency. In particular, we treat them as a two-port network and compute the scattering parameters as functions of the operational frequency f . In Fig. 3(a), we represent the magnitudes of S parameters in dB with respect to $2 \text{ GHz} < f < 3 \text{ GHz}$ for various distances b of the first antenna from the interface ($b = 100, 200, 300$ mm); the lighter the used color is, the more distant the dipole is placed. One directly observes that, due to the different size of the two antennas, the reflections are stronger in the first one compared to those at the second one; indeed, the transmitting cylindrical dipole is lengthier and thicker compared to the receiving one [40].

What is noteworthy is that both $|S_{11}|$ and $|S_{22}|$ are minimized very close to bluetooth frequency $f \cong 2.45$ GHz and in a manner not significantly dependent on the location b . Such a result is not coincidental since the characteristics of the antennas determining their resonances, have been previously optimized. As far as the transmission $|S_{21}|$ from one port to the other is concerned, it is obviously inversely proportional to the distance b since the directivities of the antennas are finite. Indeed, for increasing b , the radiated power is distributed across a larger surface and, thus, a smaller portion reaches the receiving antenna.

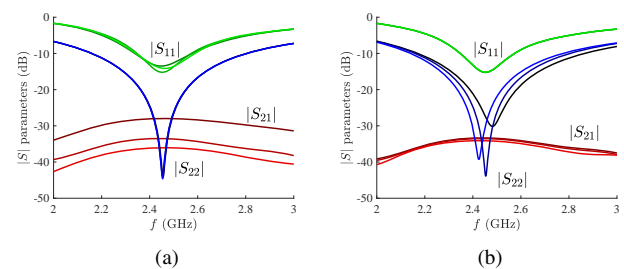


FIGURE 3. The scattering parameters magnitudes of the system of the two dipole antennas in the absence of any matching equipment for: (a) $b = 100, 200, 300$ mm with $h = 15$ mm and (b) $h = 10, 15, 20$ mm with $b = 200$ mm. The lighter the color tone of the curve is, the larger the implicit parameter is selected.

In Fig. 3(b), we show again the frequency dispersion of same quantities as in Fig. 3(a) but for several distances h of the second antenna from the human skin ($h = 10, 15, 20$ mm). Similarly to Fig. 3(a), the reflections to the first antenna are not affected substantially by the placement of the port but are still minimized at the same operational frequency, regardless of the selection of h . Moreover, $|S_{21}|$ is also practically inde-

pendent from the distance h contrary to what is happening in Fig. 3(a); this is due to the small values of h , since the receiver should stay into the fat, under human skin. Interestingly, the reflection at the second antenna changes for different values of h since the formed Fabry-Perot cavities are resonating at different frequencies; however, all the three minima of the curves are close to our working frequency $f \cong 2.45$ GHz.

B. REFLECTION COEFFICIENTS

Prior proceeding with the numerical simulations for the transferred power, it would be interesting to investigate the variation of the reflectivities as obtained in (1), (4) and test the perfect conditions obtained theoretically in (3), (5). Therefore, in Fig. 4(a), we represent the magnitude of the reflection coefficient $|R_L|$ for the analytical model of Fig. 2(a) with respect to the normalized thickness of the layer a/b and the relative permittivity of its medium ε_2 , in a contour plot. We use a fixed $b = 200$ mm even though is not a parameter of our model, so that to relate with our realistic setup of Fig. 1(a). One observes that $|R_L|$ is a periodic function of a , which is natural since condition (3) gives an infinite number of solutions ($m \in \mathbb{N}$ from (2)). The regime of minimum reflection is indicated by an \times marker which is in agreement with (3) and imposes maximal transmission into human tissue. On that variation map of $|R_L|$, we show three additional circular markers corresponding to the optimal parametric regimes of the actual configuration of Fig. 1(a), as obtained via numerical simulations. Each of them concerns a different placement h of the passive antenna, but all of them are close to the theoretical predicted one (marker \times). It is noted that, when increasing h , the realistic results come closer to the analytical solution of (3).

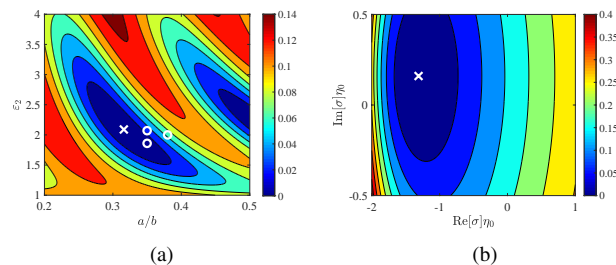


FIGURE 4. (a) The magnitude of reflection coefficient $|R_L|$ from (1) as a function of relative thickness of the layer a/b and relative complex permittivity $\varepsilon_2(1 - i0.05)$. The circular markers denote optimal operation points of the actual system of Fig. 1(a) for various locations h of receiving dipole. (b) The magnitude of reflection coefficient $|R_M|$ from (4) as a function of real and the imaginary part of the relative complex surface conductivity $\sigma\eta_0$. Plot parameters: $\varepsilon_1 \cong 5.28(1 - 0.14i)$, $b = 200$ mm. The marker \times corresponds to the parametric point of minimum reflections.

In Fig. 4(b), we depict the magnitude reflection coefficient $|R_M|$ from (4) across the complex plane of surface conductivity $\sigma\eta_0$ multiplied by the wave impedance of the space. Again, the matching regime is denoted by the \times marker which gives the $\sigma\eta_0$ indicated by (5). By inspection of Fig. 4(b), one directly remarks that the equipotential contour lines around the optimal regime, resemble perfect circles. Indeed, the demand for constant and small magnitude $|R_M| \rightarrow 0$

from (4) gives the equation of the circle: $(\text{Re}[\sigma\eta_0] - 1 + \text{Re}[\sqrt{\varepsilon_1}]^2 + (\text{Im}[\sigma\eta_0] + \text{Im}[\sqrt{\varepsilon_1}])^2 = |R_M|^2$. It is noteworthy that, given the fact that $\text{Re}[\sqrt{\varepsilon_1}] > 1$, the surface conductivity that “unlocks” the structure [14] to achieve perfect matching has a negative real part ($\text{Re}[\sigma] < 0$) which characterizes active structures. Therefore, the proposed remedy for poor coupling of Figs 1(b), 2(b) (matching layer) involves gain media. Such a feature renders it fundamentally different from the solution described by Figs 1(a), 2(a) (lossless matching metasurface) and, thus, worthy to study it. It can be also mentioned that the magnitude of the reflection coefficient $|R_M|$ may surpass unity as the amount of energy that the structure provide adds to the equilibrium; it routinely happens in parity-time symmetric configurations [41].

C. OPTIMAL MATCHING LAYERS

Having understood the ranges within which the parameters (a, ε_2) of the matching layer should belong, we again consider the actual structure of Fig. 1(a) to numerically simulate it. The key metric in understanding how much the coupling between the two radiators has been improved is the ratio of the transmitted power P'_{tran} in the presence of the matching setup over the respective power P_{tran} in the absence of them. This quantity is denoted by Q and can be also given as the ratio of the square magnitudes of the respective S_{21} quantities characterizing the two two-port networks. The definition is given below and takes into account the misalignment angles (θ, φ) only for the improved structure (numerator, primed) so that it is always compared with the best possible orientation ($\theta = \varphi = 0$) of the initial structure (denominator, unprimed).

$$Q \equiv \frac{P'_{\text{tran}}(\theta, \varphi)}{P_{\text{tran}}(\theta = 0, \varphi = 0)} \cong \frac{|S'_{21}(\theta, \varphi)|^2}{|S_{21}(\theta = 0, \varphi = 0)|^2}. \quad (6)$$

It is important to stress that the value of Q is dependent on the sequence of twisting the receiving dipole with respect to angles (θ, φ); indeed, the obtained configurations differ for a different order of rotations. However, if one covers the entire range of angles $0 < \theta, \varphi < 90^\circ$, all possible misalignment cases are considered. In our examples, we will focus on scenarios that the twist with respect to φ (if there is any) happens first, followed by the one with respect to θ (if there is any).

In Fig. 5, we represent the metric Q defined by (6) on a map similar to that of Fig. 4(a) for several placements of the primary and secondary antenna. In Fig. 5(a), typical distances are assumed ($b = 200$ mm, $h = 15$ mm) and enhancement up to 50% of the transmitted power is recorded for relatively thin layers ($a/b \cong 0.35$). In Fig. 5(b), we change the location of the receiving dipole but the variation of Q does not change much since $h/\lambda \ll 1$; however the optimal permittivity increases due to the shrunk of Fabry-Perot cavity between the air/layer boundary and the passive antenna. In Fig. 5(c), we locate the active dipole closer to the boundary (smaller $b = 100$ mm) and, naturally, the optimal operation point appears at a higher ratio a/b ; in addition, the slab permittivity ε_2 does not vary significantly compared to

Fig. 5(a) since h remains constant ($h = 15$ mm). In Fig. 5(d), we consider a more distant source ($b = 300$ mm) and obtain a similar response to that of Fig. 5(a) since the human tissue is positioned at the far field of the antenna; obviously, the highest Q emerges at a smaller a/b since b got bigger.

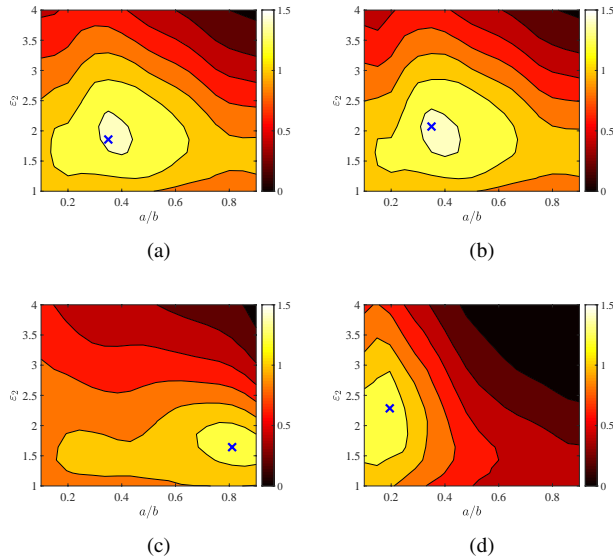


FIGURE 5. The magnitude of the metric Q from (6) as a function of relative thickness of the layer a/b and relative complex permittivity $\varepsilon_2(1 - i0.05)$. (a) $b = 200$ mm and $h = 15$ mm, (b) $b = 200$ mm and $h = 10$ mm, (c) $b = 100$ mm and $h = 15$ mm, (d) $b = 300$ mm and $h = 15$ mm. Blue \times markers denote the optimal regimes.

Unlike the transmitting antenna, which is positioned ideally into the measurement setup, the orientation of the receiving one is not controlled since it is buried into human tissue. Therefore, it is meaningful to test the performance of our matching layer with respect to arbitrary misalignment angles (θ, φ) , as defined in Fig. 1(a). In Fig. 6(a), we consider the optimal configuration from Fig. 5(a) and represent the variations $Q = Q(\theta)$ for $\varphi = 0$ and various distances b ; it is, obviously, observed that they are decreasing functions of θ . It is also remarkable that even if the two dipole directions form angles as big as $\theta = 20^\circ$, we compute $Q > 1$ which means that our matching structure remains superior than a perfectly aligned but layer-free model. In Fig. 6(b), we represent the metric Q but, this time, with respect to rotation angle φ , when keeping $\theta = 0$. Once more the curves are downward sloping due to the polarization crosstalk while the transmissivity enhancement exhibits substantial robustness with respect to angle φ . It is noteworthy, that even if the design has been optimized for $b = 200$ mm giving $Q \cong 1.4$, it works well for alternative placements of the primary source; that is another finding remarking that the proposed configurations are still beneficial for a parametrically perturbed environment.

Finally, in Fig. 6(c), we examine a receiving dipole that is simultaneously rotated by both the misalignment angles with the one by φ first, for $b = 200$ mm; to this end, we depict the distribution of $Q = Q(\theta, \varphi)$ in a contour plot. One can

observe that the highest score occurs at $\theta = \varphi = 0$, which is obviously the starting point of both the respective curves for $b = 200$ mm in Figs 6(a), 6(b). In addition, when the sum of the two twists is constant, the response Q formulate zones of similar magnitude; indeed, for $\theta + \varphi \cong 120^\circ$ the results are worse than in the case of maximally rotating the two antennas ($\theta = \varphi = 90^\circ$).

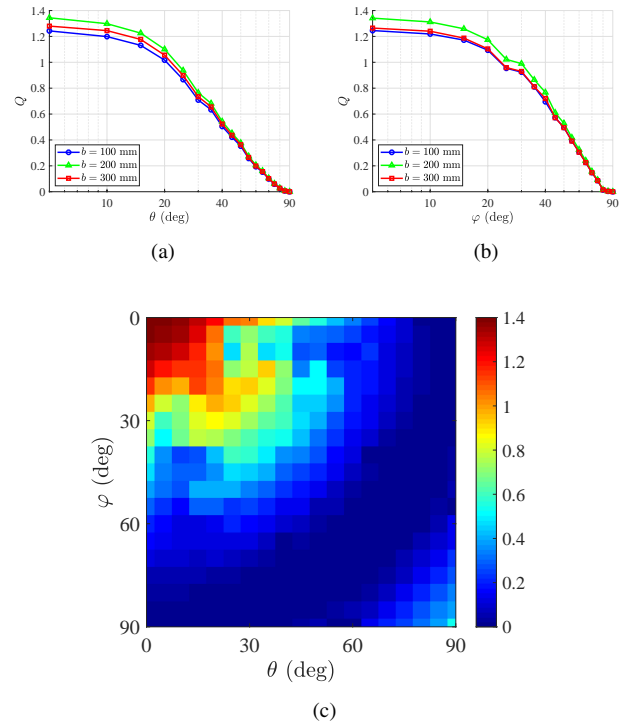


FIGURE 6. The magnitude of the metric Q from (6), in the case of the optimized matching layer (Fig. 1(a)) for $b = 200$ mm and $h = 15$ mm, as a function of: (a) dipole misalignment angle θ for $\varphi = 0$ and several distances b , (b) dipole rotation angle φ for $\theta = 0$ and several distances b , and (c) both misalignment angles (θ, φ) in contour plot. Plot parameters: $\varepsilon_2 \cong 1.86$, $a \cong 0.35b$ from Fig. 5(a).

D. OPTIMAL MATCHING METASURFACES

It would be interesting to observe the operation of deposited metasurfaces in an attempt to maximize Q , as defined from (6), in the actual system of dipoles. Given the fact that in our theoretical model of Fig. 2(b), the perfect matching occurred for $\text{Re}[\sigma] < 0$, according to (5) and Fig. 4(b), we will not rule out the usage of gain media in our simulations. Therefore, in Fig. 7(a), we represent Q (in dB) across the complex plane of surface conductivity $\sigma = \text{Re}[\sigma] + i \text{Im}[\sigma]$ and realize that a huge transmissivity enhancement of more than two orders of magnitude becomes feasible, which is attributed exactly to the active nature of the employed matching approach. It is noticeable that the emerged peak of Fig. 7(a) is accompanied by an anti-resonance, yielding minimum Q nearby, revealing an anticipated Fano resonance pattern.

One may wonder why the optimal operation point does not coincide with the corresponding one of the analytical model in Fig. 2(b), contrary to the apparent similarity between

Figs 4(a), 5(a) when the matching layer was used instead. The answer lies again in the fact that the optimal layer is passive while the most efficient metasurfaces require gain materials. Indeed, the reflectivity and the transmissivity are not any more complementary each other; as a result, an active metasurface can support giant transmission accompanied by significant reflections. In this sense, our metasurface strategy does not concern matching the free space with the human tissue but aims at optimally amplifying the incoming signal so that maximum penetration is achieved.

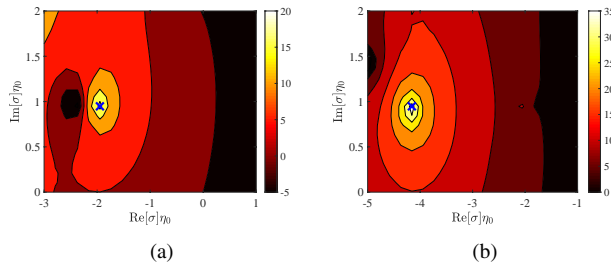


FIGURE 7. The magnitude of the metric Q from (6) in dB across the complex plane of the dimensionless surface conductivity of the metasurface ($\text{Re}[\sigma]_{\eta_0}$, $\text{Im}[\sigma]_{\eta_0}$). (a) $b = 200$ mm and $h = 15$ mm, (b) $b = 100$ mm and $h = 15$ mm. Blue \times markers denote the optimal regimes.

In Fig. 7(b), we repeat the same calculations as in Fig. 7(a) but for a transmitting antenna located closer to human tissue ($b = 100$ mm). It is remarked that Q reaches much higher magnitudes compared to Fig. 7(a); that finding could be anticipated since the primary source is positioned near an active medium which, in turn, acts a secondary source that pumps new energy to the system. When it comes to the influence of gain $\text{Re}[\sigma]$ on our observable Q , it is not necessarily positive. In the same way that increasing losses do not automatically mean increasing absorption, there are optimal ranges of gain that give substantial Q values. Indeed, for more negative real part of conductivity ($|\text{Re}[\sigma] < 0$) than the one corresponding to the maximum of Fig. 7(b), the performance of the respective metasurface is particularly poor, which validates the aforementioned point. As far as the imaginary part of σ is concerned, it just gives capacitive or inductive role to the metasurface and pushes it towards the reported resonances.

In Fig. 8, we redo the calculations of Fig. 6 but when the optimally designed active metasurfaces are used from Fig. 7. In Fig. 8(a), we observe the metric Q of the optimal metasurface as a function of misalignment angle θ with $\varphi = 0$, for various locations b of the external dipole. Giant scores are recorded not only with $b = 200$ mm (for which the setup has been optimized) but also with $b = 300$ mm for most of the directions within the cone $0 < \theta < 40^\circ$, due to the active nature of the used equipment. On the contrary, the performance drops if $b = 100$ mm, even though the transmissivity enhancement reaches giant magnitudes in Fig. 7(b); indeed, the employed metasurface does not work optimally for $b = 100$ mm.

In Fig. 8(b), we represent the score Q for the same structure

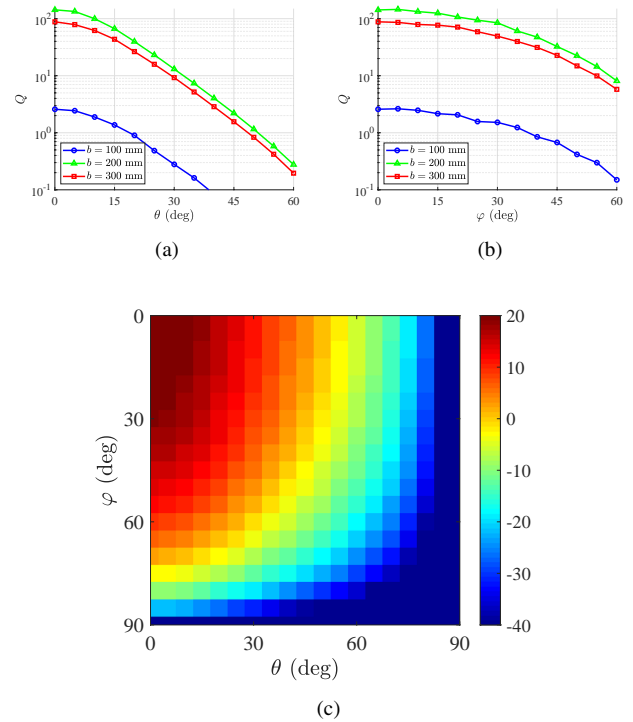


FIGURE 8. The magnitude of the metric Q from (6), in the case of the optimized matching metasurface (Fig. 1(b)) for $b = 200$ mm and $h = 15$ mm, as a function of: (a) dipole misalignment angle θ for $\varphi = 0$ and several distances b , (b) dipole rotation angle φ for $\theta = 0$ and several distances b , and (c) both misalignment angles (θ , φ) in contour plot and Q expressed in dB. Plot parameters: $\sigma_{\eta_0} \cong -1.95 + 0.95i$ from Fig. 7(a).

as in Fig. 8(a) (optimized for $b = 200$ mm), as a function of the rotation angle φ by keeping $\theta = 0$. Apparently, the starting points of the three curves are the same as in Fig. 8(a) since they all refer to aligned dipoles ($\theta = \varphi = 0$). However, the performance deteriorates much milder when modifying angle φ since the receiving dipole is rotated with respect to it first, by remaining parallel to the interface. In particular, we obtain at 10-fold enhancement for $\varphi = 60^\circ$ where the illuminating antenna is placed at $b = 200$ mm. Similarly high score is recorded for $b = 300$ mm; on the contrary, a dipole located at $b = 100$ mm, is being “suffocated” [42] due to the close distance from the interface.

In Fig. 8(b), we repeat the calculations of Fig. 6(c) and consider simultaneous twists of the buried dipole with respect to both (θ , φ). The metric Q is expressed in dB and the asymmetry of the pattern demonstrates once again the increased robustness of the effect for φ twists compared to the case of equal θ twists. Given the fact that the metasurface is infinitely thin, the more you rotate the dipole, regardless of the way (θ , φ), the obtained outcome worsens gradually; such a feature is not the case for the matching layer of Fig. 6(c). Interestingly, the considered metasurface can deliver an enhanced transmissivity ($Q > 1$) even if both misalignment angles are significant: $0 < \theta, \varphi < 45^\circ$. In fact, we exploit the activity of the structure to boost the coupling between the

two antennas without practically caring about the orientation of the receiving one; such a finding can relax the requirements for parallel dipoles in a real-world setup.

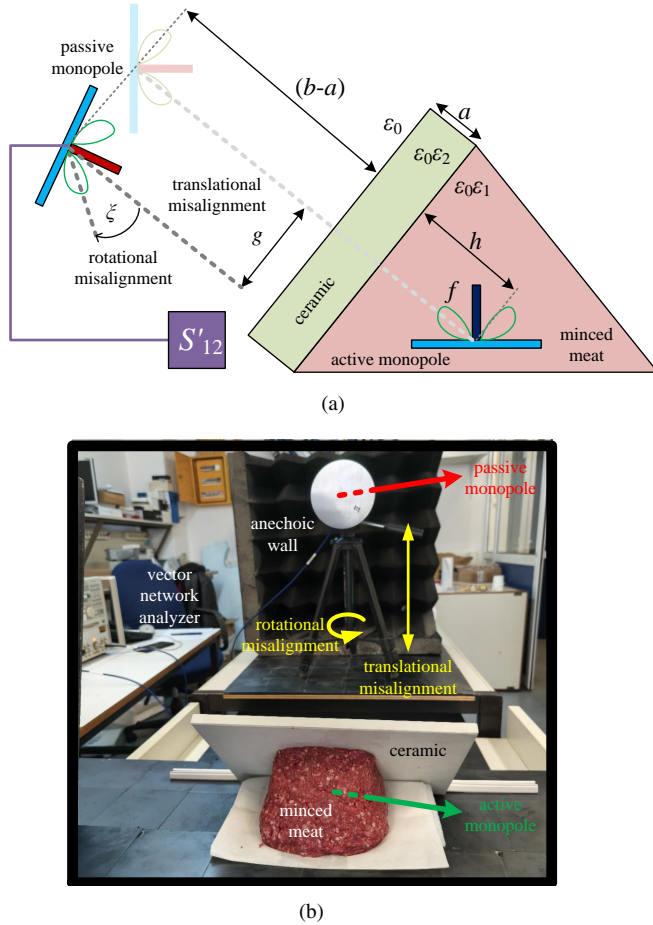


FIGURE 9. (a) Sketch of the experimental setup: a ceramic layer is deposited on minced meat which plays the role of human tissue to enhance the interaction between a passive external monopole and an active internal one. (b) Photo of the actual measurement setup. Translational and rotational misalignment is supported in accordance to Fig. 9(a). The recording vector network analyzer (VNA) measures the transmission coefficients in the absence S_{12} and in the presence S'_{12} of the matching layer.

IV. EXPERIMENTAL DEMONSTRATION

A. EXPERIMENTAL SETUP

To experimentally test the proposed concept of matching layer, we consider the measuring design of Fig. 9(a). As sources, two monopoles backed by PEC disks are used to make dipolar radiation patterns that are usually directing their maximum emitting power between the metallic base and the wire, as shown in Fig. 9(a). In this way, an optimal orientation is formed between the external active antenna and the passive counterparts that is embedded in human tissue. With respect to this regime, translational misalignment of length g and rotational misalignment by angle ξ can be defined as in Fig. 9(a). In the considered scenario, the primary source is located below human skin unlike to what was the case

in our previous theoretical examples where the structure got externally illuminated. Such a choice has been made since the measurement at the free-standing port is easier while leaving unchanged the enhancement metric, due to EM reciprocity. In other words, we evaluate the ratio:

$$Q \equiv \frac{P'_{\text{tran}}(g, \xi)}{P_{\text{tran}}(g=0, \xi=0)} \cong \frac{|S'_{12}(g, \xi)|^2}{|S_{12}(g=0, \xi=0)|^2}, \quad (7)$$

which is very similar to the one defined in (6). Between the two custom-made antennas and on the human tissue of relative permittivity ε_1 , we deposit a ceramic layer of thickness a and relative permittivity ε_2 .

As stated before, we assume a frequency at the bluetooth band, namely, $2.3 \text{ GHz} < f < 2.7 \text{ GHz}$ with a central one of $f \cong 2.45 \text{ GHz}$ ($\lambda \cong 12.25 \text{ cm}$). The active source is buried into the meat at $h \cong 7 \text{ cm}$ while the passive antenna is placed at distance $(b-a) \cong 62 \text{ cm}$ for reasons related to the calibration of the antennas elaborated in Subsection IV-B. The role of human tissue is played by minced meat whose permittivity of several samples has been measured at $\varepsilon_1 \cong 22$, via the process described in Subsection IV-C. By imposing the matching condition (2), the thinnest design corresponds to $a \cong 1.4 \text{ cm}$ with $\varepsilon_2 \cong 4.7$. The closest available material of such characteristics at $f \cong 2.45 \text{ GHz}$, is a ceramic, hydrocarbon polymer [43], as explained in Subsection IV-C. That material is characterized by a dielectric constant $\varepsilon_2 = 4.515$ while the size of the employed block has been measured equal to: $a = 1.27 \text{ cm}$; that was the closest parameter set we could found to that dictated by the zero reflections regime (2). A photo of the experimental setup is shown in Fig. 9(b), where translational (g) and rotational (ξ) pointing error can be emulated. The transmission coefficients are measured by the vector network analyzer (VNA) in the presence of a background anechoic wall made of a suitable absorbing material and the results are presented in Subsection IV-D.

An oblique boundary between the ceramic layer and the minced meat has been selected in Fig. 9(a) so that the heavy dielectric plate avoid pressing destructively the meat. The final customized measurement setup is shown in Fig. 10(a), where ferrite plates are placed at the bottom and anechoic walls around the radiators to eliminate any possible reflections from the surrounding environment. The terminal antenna is positioned as indicated in Fig. 10(a), while the radiating rod form a 90-degree angle with the aforementioned direction in order for the optimal orientation between the two radiation patterns is achieved. The final height of the receiver is 34.5 cm, and the direct distance between the transmitting and receiving antennas equals to 70 cm (measured from the center of the monopoles).

The ground plane of the transmitting monopole sits on a 5 mm minced meat layer as shown in Fig. 10(b) and then we firmly attach the antenna on top to cover it fully with the rest of the meat, as designated in Fig. 10(c). Initially, we measure the transmission coefficient (S_{21}) without the matching material, as indicated by Fig. 10(c). The measurements are

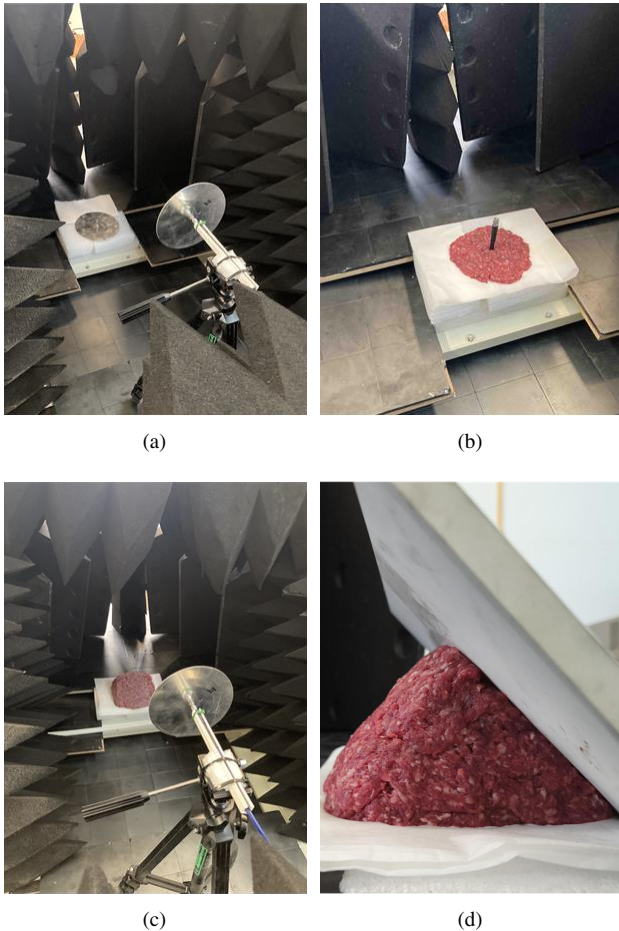


FIGURE 10. Pre-measurements preparations. (a) Alignment measurements. (b) Minced meat below the ground plane. (c) Measurements without the matching layer. (d) Matching layer attached to the minced meat.

repeated by placing carefully and firmly the dielectric plate, as shown in Fig. 10(d), where S'_{21} is measured again. In this way, the quantity of (7) is evaluated.

B. MONOPOLE ANTENNAS CALIBRATION

All the measurements (either for transmission or reflection coefficient) are carried out using a four-port vector network analyzer (Agilent N5230 PNA-L), and two identical two-meter-long cables (Mini Circuits FLC-2M-SMSM+) with an insertion loss of 1.0-1.5 dB across our frequency band of interest. Prior to measurements, a back-to-back calibration is performed utilizing an electronic calibration module (Agilent N4331-60006) for de-embedding the cables and removing unwanted nonlinearities induced by the system. The intermediate frequency, the sweep time, the number of sample points and the averaging parameters that are used in that process are selected according to proper handbooks [44].

A monopole antenna is designed and simulated with Empire XPU tool [45], so that it resonates around the well-known bluetooth frequency. The specific antenna can be easily fabricated by simple materials and implanted without igniting

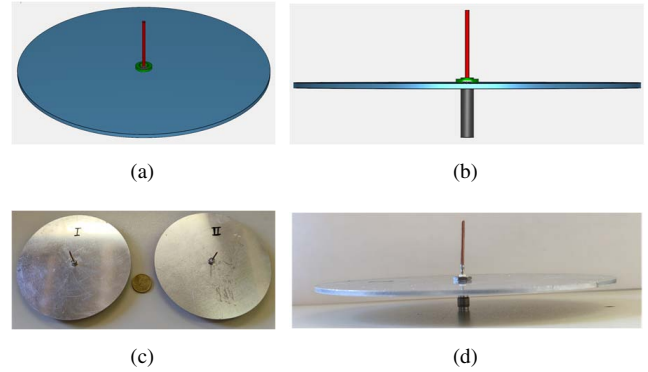


FIGURE 11. Experimental monopole antennas. (a) Three-dimensional view of the used design. (b) Side view of the used design. (c) Fabricated transmitting and receiving antennas. (d) Side view of the fabricated antenna.

significant coupling effects with the emulated tissue. Figs 11(a), 11(b) depict the three dimensional and the side view of the designed antennas, which need an infinite ground plane [46]. To achieve a minimum reflection coefficient ($|S_{11}|$) at 2.45 GHz, the active antenna is taken with a metallic ground plane with a diameter of 14 cm and thickness of 1 mm. As far as the radiating rod is concerned, it is designed with a length of 29.2 mm and a diameter of 1.77 mm, in accordance with [47].

The final custom-made fabricated monopole antennas are shown in Fig. 11(c). The ground plane is constructed with galvanized steel, having the aforementioned dimensions, and the radiating rod is made from a typical 2.5 mm^2 wire cable soldered to the sub-miniature version A (SMA) connector, as implied in Fig. 11(d). To tune the resonant frequency as close as possible to the simulated one, the radiated rod is chosen about 25 mm long. The maximum simulated gain is equal to 3.6 dBi achieved at an elevation angle of 45° , as indicated in Fig. 12(a) (the vertical axis corresponds to the metallic disk). The azimuth pattern is omnidirectional and the -10 dB bandwidth is close to 550 MHz with the final resonant frequency at 2.453 GHz exhibits a reflection coefficient $|S_{11}|$ less than -40 dB, according to Fig. 12(b). Both the antennas achieve finally $|S_{11}|$ smaller than -26 dB at the two almost identical frequencies 2.467 GHz and 2.462 GHz, as demonstrated by Fig. 12(b).

C. PERMITTIVITY MEASUREMENT

A key feature in deciding the exact characteristics of the matching layer is the (unknown, up to that point) permittivity of the substance used to mimic the human tissue. Only with a reliable estimation for ϵ_1 , we will be able to evaluate the dielectric constant ϵ_2 and the thickness a of the dielectric plate. The related measurement setup is based on a transverse electric magnetic (TEM) transmission line. A rectangular metal cavity, shown in Fig. 13(a), is penetrated by a wire that connects the center conductors of two panel SMA connectors mounted on the opposite walls of the cavity. Its outer and

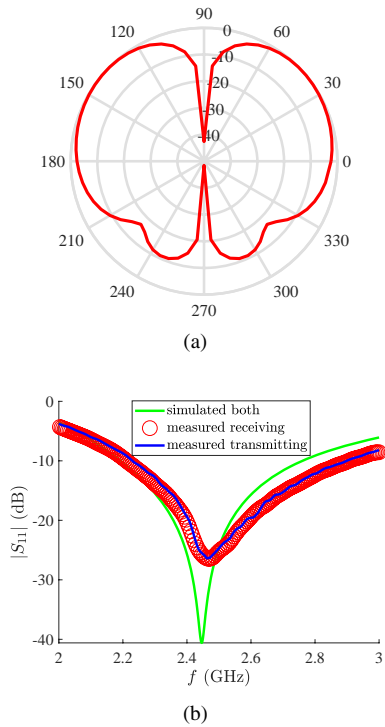


FIGURE 12. Simulations and measurements for monopole antennas. (a) Simulated antenna pattern in dB. (b) Simulated and measured reflection coefficients.

inner dimensions read: 51.9 mm × 32.3 mm × 33.6 mm and 40.4 mm × 20.9 mm × 20.0 mm, respectively.

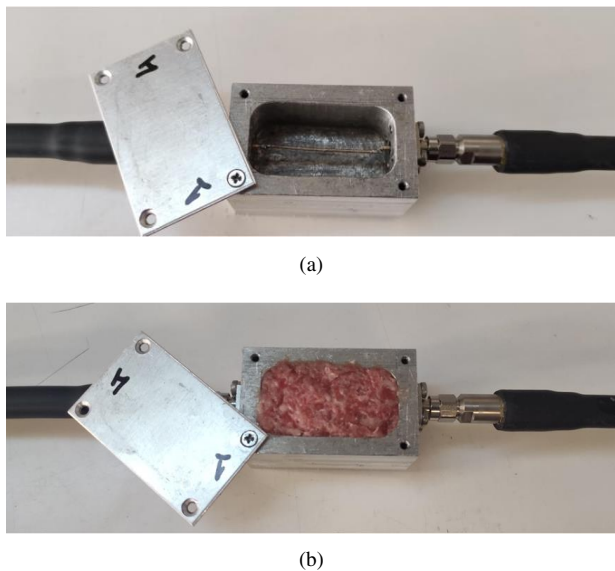


FIGURE 13. Setups for the permittivity measurements of minced meat. (a) Empty cavity. (b) Filled cavity.

A differential measurement of the transmission phase is performed with and without the material-under-test (MUT) using the VNA; such a phase shift allows for determining the real part of the complex permittivity of the material filling the cavity [44]. Indeed, the transmission line supports the

TEM fundamental propagating mode and the presence of the dielectric sample affects the wavenumber (phase constant) of the developed wave [48]. More specifically, the phase constant is proportional to the refractive index of the MUT [49], [50]. An approximation behind this measurement method is that the medium occupies the cavity in a uniform manner and fully surrounding the inner wire without leaving any air pockets. Every possible effort is made in this direction during the samples preparation, as shown in Fig. 13(b).

The average phase difference from the five samples is found equal to 4.7; hence, the calculated dielectric constant is found close to $\epsilon_1 = 4.7^2 = 22.09 \Rightarrow \epsilon_1 \cong 22$, which is a good approximation between the respective values [51] for pure fat ($\epsilon = 5.5$) and muscle ($\epsilon = 49$). If one imposes the constraints (3) for perfect matching with the aforementioned ϵ_1 , it is clear that the reflections are minimized when the permittivity of the utilized layer reads: $\epsilon_2 \cong 4.7$, as mentioned in Subsection IV-A. When it comes to the thickness of the dielectric, it is evaluated as 1.4 cm, once working at the resonant frequency of 2.45 GHz. As also stated in the Subsection IV-A, the best-found commercial material with such an electrodynamic behavior is the polymer composite Rogers TMM4 [43] with $\epsilon_2 = 4.515$ while the closest available layer thickness of a sample was 1.27 cm.

D. EFFICIENT POWER TRANSFER

Having concluded to all the parameters that experimentally realize our theoretical concept, we are ready to evaluate Q from (7). Our measurement scenarios involve rotational (angle ξ in Fig. 9(a)) and translational (transverse distance g in Fig. 9(a)) misalignment, having the optimally matching dielectric layer (for $\xi = 0$ and $g = 0$) being attached to the minced meat. Translational tests are carried out elevating the receiver height from 0 cm up to 20 cm in steps of 5 cm (while keeping $\xi = 0$); the results are depicted in Fig. 14(a). The receiving antenna orientation is then adjusted, tilted downwards from 0 to 50° in steps of 10° (while keeping $g = 0$); the results are depicted in Fig. 14(b). The separating distance between transmitter and receiver remained constant during those tests.

Therefore, in Fig. 14(a), we present the enhancement metric from (7) in dB with respect to oscillating frequency f for several translational pointing errors g with zero rotational misalignment ($\xi = 0$). It is clear that the matching ceramic layer increases the transmitted power across the entire band even if the two antennas are not facing each other. Obviously, the emitted power P'_{tran} decreases with g but it remains larger compared to P_{tran} corresponding to the scenario that $g = 0$ but without matching slab. The only exception is made by the curve taken for $b = 20$ cm where the line of sight lies completely outside of main lobes of the two antennas and yields in a deterioration of the transmitted signal magnitude.

Similarly, in Fig. 14(b), we repeat the same calculations as in Fig. 14(a) but with zero translational misalignment ($g = 0$), for several rotational pointing error angles ξ . It is clear that once ξ is kept small, almost no harm is done to the wireless link between the two monopoles. But even

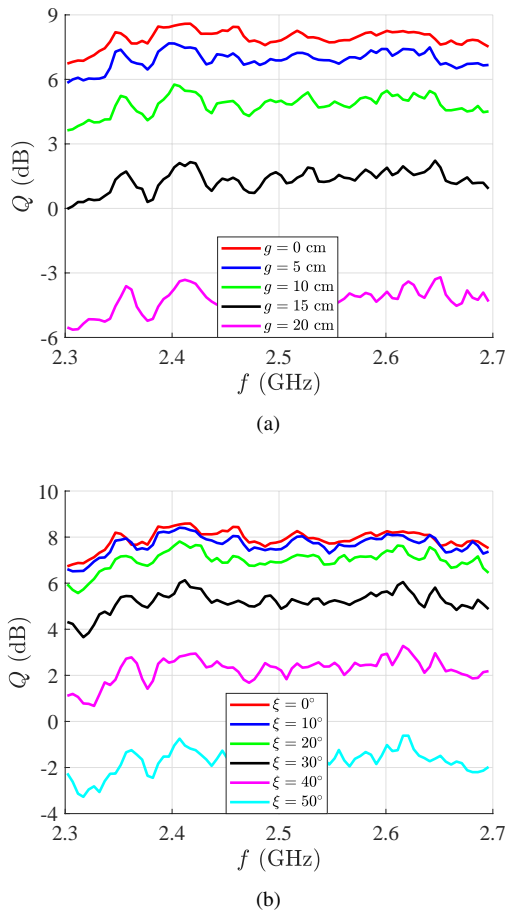


FIGURE 14. The enhancement metric Q as defined by (7) in dB as a function of the operational frequency f : (a) for several translational misalignment g (with $\xi = 0$), (b) for several rotational misalignment ξ (with $g = 0$).

when ξ takes substantial values, wideband enhancement is reported when the ceramic layer is placed in-between. As happens in Fig. 14(a), we obtain $P'_{\text{tran}} < P_{\text{tran}}$ only for the worst scenario ($\xi = 50^\circ$) where we fail to exploit the gain of the two antennas. According to the measurement results of Fig. 14, a noticeable improvement in $|S_{21}|$ is observed for two well-aligned radiators ($\xi = 0$ and $g = 0$). In particular, the Q factor is found more than 8.2 dB, on average, at the resonant frequency of 2.46 GHz, thus justifying the theoretical expectations of the proposed concept.

V. CONCLUSIONS

External electromagnetic sources can be matched with implanted antennas into human tissue by tuning the operational frequency so that minimal reflections are achieved. While keeping the oscillating wavelength unaltered, we investigate the possibility of improving further the coupling between the two dipoles by depositing dielectric layers or metasurfaces across the air/skin interface. An equivalent one-dimensional semi-analytical model indicates that, at bluetooth band, the optimal layer is an ordinary quarter-wavelength transformer

but the optimal metasurface is an active one. Therefore, the two matching strategies are fundamentally different each other but each one possesses certain unique advantages: the former one nullifies the reflections back to the source while the latter one can hugely boost transmissivity into the human skin. Extensive numerical simulations of the actual, three-dimensional systems validate the expected outcomes while the coupling performance of each layout has been tested successfully against misalignment of dipoles axes that cause polarization crosstalk. Our results, that have been validated in the laboratory, may inspire further experimental efforts towards more efficient communication with implantable antennas that are supporting high data rates while being harmless for the patient.

An interesting expansion of the present work would be to focus on which media or meta-atoms can be used to build the proposed matching layers that are operable at the same frequencies and remedy potential availability limitations. Moreover, one can use instead of wireless sources, wires connected with the equipment that is wrapped around the human skin and, in this way, materialize an analogue of active metasurface. Similar analytical and numerical techniques as the ones employed in this work may be implemented to understand the interference between the multiple sources that secures strong transmissivity into the human body. Due to reciprocity they will give a clearer picture about the structural and textural formations below the skin. In this way, a variety of minimally invasive biomedical processes can become easier to provide real-time information from the glucose content and the blood pressure to the distribution of virions or the size of protein cells.

REFERENCES

- [1] A. Kiourti and K. S. Nikita, "A Review of Implantable Patch Antennas for Biomedical Telemetry: Challenges and Solutions," *IEEE Antennas Propag. Mag.*, vol. 54, no. 3, pp. 210–228, Jun. 2012, doi: 10.1109/MAP.2012.6293992.
- [2] A. Kiourti and K. S. Nikita, "A Review of In-Body Biotelemetry Devices: Implantables, Ingestibles, and Injectables," *IEEE Trans. Biomed. Eng.*, vol. 64, no. 7, pp. 1422–1430, Jul. 2017, doi: 10.1109/TBME.2017.2668612.
- [3] A. Kiourti, K. A. Psathas, and K. S. Nikita, "Implantable and ingestible medical devices with wireless telemetry functionalities: a review of current status and challenges," *Bioelectromagnetics*, vol. 35, no. 1, pp. 1–15, Jan. 2014, doi: 10.1002/bem.21813.
- [4] T. Karacolak, A. Z. Hood and E. Topsakal, "Design of a Dual-Band Implantable Antenna and Development of Skin Mimicking Gels for Continuous Glucose Monitoring," *IEEE Trans. Microw. Theory Tech.*, vol. 56, no. 4, pp. 1001–1008, Apr. 2008, doi: 10.1109/TMTT.2008.919373.
- [5] M. L. Scarpello, D. Kurup, H. Rogier, D. V. Ginste, F. Axisa, J. Vanflteren, W. Joseph, L. Martens, and G. Vermeeren, "Design of an Implantable Slot Dipole Conformal Flexible Antenna for Biomedical Applications," *IEEE Trans. Antennas Propag.*, vol. 59, no. 10, pp. 3556–3564, Jul. 2011, doi: 10.1109/TAP.2011.2163761.
- [6] T. Karacolak, R. Cooper, and E. Topsakal, "Electrical Properties of Rat Skin and Design of Implantable Antennas for Medical Wireless Telemetry," *IEEE Trans. Antennas Propag.*, vol. 57, no. 9, pp. 2806–2812, Sep. 2009, doi: 10.1109/TAP.2012.2201078.
- [7] A. Kiourti and K. S. Nikita, "Miniature Scalp-Implantable Antennas for Telemetry in the MICS and ISM Bands: Design, Safety Considerations and Link Budget Analysis," *IEEE Trans. Antennas Propag.*, vol. 60, no. 8, pp. 3568–3575, Dec. 2012, doi: 10.1109/TAP.2012.2201078.
- [8] C. Liu, Y.-X. Guo, H. Sun, and S. Xiao, "Design and Safety Considerations of an Implantable Rectenna for Far-Field Wireless Power Transfer," *IEEE*

- Trans. Antennas Propag.*, vol. 62, no. 11, pp. 5798–5806, Aug. 2014, doi: 10.1109/TAP.2014.2352363.
- [9] A. Kiourti, J. R. Costa, C. A. Fernandes, and K. S. Nikita, “A Broadband Implantable and a Dual-Band On-Body Repeater Antenna: Design and Transmission Performance,” *IEEE Trans. Antennas Propag.*, vol. 62, no. 6, pp. 2899–2908, Jun. 2014, doi: 10.1109/TAP.2014.2310749.
- [10] C. Liu, Y.-X. Guo, and S. Xiao, “Capacitively Loaded Circularly Polarized Implantable Patch Antenna for ISM Band Biomedical Applications,” *IEEE Trans. Antennas Propag.*, vol. 62, no. 5, pp. 2407–2417, Feb. 2014, doi: 10.1109/TAP.2014.2307341.
- [11] X. Y. Liu, Z. T. Wu, Y. Fan, and E. M. Tentzeris, “A Miniaturized CSRR Loaded Wide-Beamwidth Circularly Polarized Implantable Antenna for Subcutaneous Real-Time Glucose Monitoring,” *IEEE Antennas Wirel. Propag. Lett.*, vol. 16, pp. 577–580, 2017, Jul. 2016, doi: 10.1109/LAWP.2016.2590477.
- [12] Y. Yao, R. Shankar, P. Rauter, Y. Song, J. Kong, M. Loncar, and F. Capasso, “High-Responsivity Mid-Infrared Graphene Detectors with Antenna-Enhanced Photocurrent Generation and Collection,” *Nano Lett.*, vol. 14, no. 7, pp. 3749–3754, Jul. 2014, doi: 10.1021/nl500602n.
- [13] M. S. Sharawi, “Current Misuses and Future Prospects for Printed Multiple-Input, Multiple-Output Antenna Systems,” *IEEE Antennas Propag. Mag.*, vol. 59, no. 2, pp. 162–170, Apr. 2017, doi: 10.1109/MAP.2017.2658346.
- [14] C. A. Valagiannopoulos, N. L. Tsitsas, and A. H. Sihvola, “Unlocking the Ground: Increasing the Detectability of Buried Objects by Depositing Passive Superstrates,” *IEEE Trans. Geosci. Remote Sens.*, vol. 54, no. 6, pp. 3697–3709, Jun. 2016, doi: 10.1109/TGRS.2016.2525733.
- [15] Y.-J. Lee, D. S. Ruby, D. W. Peters, B. B. McKenzie, and J. W. P. Hsu, “ZnO Nanostructures as Efficient Antireflection Layers in Solar Cells,” *Nano Lett.*, vol. 8, no. 5, pp. 1501–1505, May 2008, doi: 10.1021/nl080659j.
- [16] J. Zhu, Z. Yu, G. F. Burkhard, C.-M. Hsu, S. T. Connor, Y. Xu, Q. Wang, M. McGehee, S. Fan, and Y. Cui, “Optical Absorption Enhancement in Amorphous Silicon Nanowire and Nanocone Arrays,” *Nano Lett.*, vol. 9, no. 1, pp. 279–282, Jan. 2009, doi: 10.1021/nl802886y.
- [17] A. Kurs, A. Karalis, R. Moffatt, J. D. Joannopoulos, P. Fisher, and M. Soljačić, “Wireless Power Transfer via Strongly Coupled Magnetic Resonances,” *Science*, vol. 317, no. 5834, pp. 83–86, Jul. 2007, doi: 10.1126/science.1143254.
- [18] Z. Popović, E. A. Falkenstein, D. Costinett, R. Zane, “Low-Power Far-Field Wireless Powering for Wireless Sensors,” *Proc. IEEE*, vol. 101, no. 6, pp. 1397–1409, Jun. 2017, doi: 10.1109/JPROC.2013.2244053.
- [19] J. F. Villena, A. G. Polimeridis, Y. Eryaman, E. Adalsteinsson, L. L. Wald, J. K. White, and L. Daniel, “Fast Electromagnetic Analysis of MRI Transmit RF Coils Based on Accelerated Integral Equation Methods,” *IEEE Trans. Biomed. Eng.*, vol. 63, no. 11, pp. 2250–2261, Nov. 2016, doi: 10.1109/TBME.2016.2521166.
- [20] H. Basaeri, D. B. Christensen, and S. Roundy, “A review of acoustic power transfer for bio-medical implants,” *Smart Mater. Struct.*, vol. 25, no. 12, p. 123001, Aug. 2016, doi: 10.1088/0964-1726/25/12/123001.
- [21] N. Yu, P. Genevet, M. A. Kats, F. Aieta, J.-P. Tetienne, F. Capasso, and Z. Gaburro, “Light Propagation with Phase Discontinuities: Generalized Laws of Reflection and Refraction,” *Science*, vol. 334, no. 6054, pp. 333–337, Oct. 2011, doi: 10.1126/science.1210713.
- [22] Z. Li, M.-H. Kim, C. Wang, Z. Han, S. Shrestha, M. Lu, A. Stein, A. M. Agarwal, M. Lončar, and N. Yu, “Controlling propagation and coupling of waveguide modes using phase-gradient metasurfaces,” *Nat. Nanotechnol.*, vol. 12, no. 7, pp. 675–683, Jul. 2017, doi: 10.1038/nnano.2017.50.
- [23] J. C. Soric, R. Fleury, A. Monti, A. Toscano, F. Bilotti, and A. Alù, “Controlling Scattering and Absorption With Metamaterial Covers,” *IEEE Trans. Antennas Propag.*, vol. 62, no. 8, pp. 4220–4229, Dec. 2014, doi: 10.1109/TAP.2014.2322891.
- [24] F. Qin, L. Ding, L. Zhang, F. Monticone, C. C. Chum, J. Deng, S. Mei, Y. Li, J. Teng, M. Hong, S. Zhang, A. Alù, C.-W. Qiu, “Hybrid bilayer plasmonic metasurface efficiently manipulates visible light,” *Sci. Adv.*, vol. 2, no. 1, p. e1501168, Jan. 2016, doi: 10.1126/sciadv.1501168.
- [25] C. Valagiannopoulos, T. A. Tsiftsis, and V. Kovanis, “Metasurface-enabled interference mitigation in visible light communication architectures,” *J. Opt.*, vol. 21, no. 11, p. 115702, Jul. 2019, doi: 10.1088/2040-8986/ab4c08.
- [26] C. H. Chu, M. L. Tseng, J. Chen, P. C. Wu, Y.-H. Chen, H.-C. Wang, T.-Y. Chen, W. T. Hsieh, H. J. Wu, G. Sun, and D. P. Tsai, “Active dielectric metasurface based on phase-change medium,” *Laser Photonics Rev.*, vol. 10, no. 6, pp. 986–994, 2016, doi: 10.1002/lpor.201600106.
- [27] J. Lee, M. Tymchenko, C. Argyropoulos, P.-Y. Chen, F. Lu, F. Demmerle, G. Boehm, M.-C. Amann, A. Alù, and M. A. Belkin, “Giant nonlinear response from plasmonic metasurfaces coupled to intersubband transitions,” *Nature*, vol. 511, no. 7507, pp. 65–69, Jul. 2014, doi: 10.1038/nature13455.
- [28] M. A. Kats and F. Capasso, “Optical absorbers based on strong interference in ultra-thin films,” *Laser Photonics Rev.*, vol. 10, no. 5, pp. 735–749, 2016, doi: 10.1002/lpor.201600098.
- [29] T. A. Tsiftsis, C. Valagiannopoulos, H. Liu, A.-A. A. Boulogeorgos, and N. I. Miridakis, “Metasurface-Coated Devices: A New Paradigm for Energy-Efficient and Secure 6G Communications,” *IEEE Veh. Technol. Mag.*, vol. 17, no. 1, pp. 27–36, Mar. 2022, doi: 10.1109/MVT.2021.3119282.
- [30] Z. Li, X. Tian, C.-W. Qiu, and J. S. Ho, “Metasurfaces for bioelectronics and healthcare,” *Nat. Electron.*, vol. 4, no. 6, pp. 382–391, Jun. 2021, doi: 10.1038/s41928-021-00589-7.
- [31] M. L. Tseng, Y. Jahani, A. Leitis, and H. Altug, “Dielectric Metasurfaces Enabling Advanced Optical Biosensors,” *ACS Photonics*, vol. 8, no. 1, pp. 47–60, Jan. 2021, doi: 10.1021/acsp Photonics.0c01030.
- [32] C. Valagiannopoulos and A. Sihvola, “Maximal interaction of electromagnetic radiation with corona virions,” *Phys. Rev. B*, vol. 103, no. 1, p. 014114, Jan. 2021, doi: 10.1103/PhysRevB.103.014114.
- [33] V. Mouzi, “Maximal coupling between implanted dipole antennas and external sources,” National Technical University of Athens, Master Program on Translational Engineering in Health and Medicine, Master Thesis, 2025, doi: 10.26240/heal.ntua.28368.
- [34] C. Valagiannopoulos, “Closed-form solution to the scattering of a skew strip field by metallic pin in a slab,” *Prog. Electromagn. Res.*, pp. 1–21, Jan. 2008, doi: 10.2528/PIER07092206.
- [35] C. A. Valagiannopoulos and N. L. Tsitsas, “Integral equation analysis of a low-profile receiving planar microstrip antenna with a cloaking superstrate,” *Radio Sci.*, vol. 47, no. 2, 2012, doi: 10.1029/2011RS004878.
- [36] C. Valagiannopoulos, A. Sarsen, and A. Alù, “Angular Memory of Photonic Metasurfaces,” *IEEE Trans. Antennas Propag.*, vol. 69, no. 11, p. 7720, Nov. 2011, doi: 10.1109/TAP.2021.3083806.
- [37] S. Maity, K. R. Barman, and S. Bhattacharjee, “Silicon-based technology: Circularly polarized microstrip patch antenna at ISM band with miniature structure using fractal geometry for biomedical application,” *Microw. Opt. Technol. Lett.*, vol. 60, no. 1, pp. 93–101, Jan. 2018, doi: 10.1002/mop.30925.
- [38] D. Gopi, K. Kumar Naik, and S. Rani, “Design of ISM Band CPW-fed SRR Patch Conformal Antenna for Bio-medical Applications,” *IEEE Access*, vol. 7, pp. 1–1, Mar. 2019, doi: 10.1109/ACCESS.2019.2905661.
- [39] C. A. Klingenbock, T. Samaras, C. Goiceanu, and N. Kuster, “The dependence of electromagnetic far-field absorption on body tissue composition in the frequency range from 300 MHz to 6 GHz,” *IEEE Trans. Microw. Theory Tech.*, vol. 54, no. 5, pp. 2188–2195, Feb. 2006, doi: 10.1109/TMTT.2006.872789.
- [40] G. Fikioris and C. Valagiannopoulos, “Input admittances arising from explicit solutions to integral equations for infinite-length dipole antennas,” *Prog. Electromagn. Res.*, vol. 55, pp. 285–306, Jan. 2005, doi: 10.2528/PIER05031701.
- [41] C. A. Valagiannopoulos, F. Monticone, and A. Alù, “PT-symmetric planar devices for field transformation and imaging,” *J. Opt.*, vol. 18, no. 4, p. 044028, Dec. 2016, doi: 10.1088/2040-8978/18/4/044028.
- [42] A. Aitbayev and C. Valagiannopoulos, “Hiding a Light Source with Photonic Dimers of Paired Nanorods,” *IEEE Trans. Antennas Propag.*, vol. 74, no. 1, p. 841, Jan. 2024, doi: 10.1109/TAP.2023.3329951.
- [43] S. E. Morris, Y. Bayram, L. Zhang, Z. Wang, M. Shtein, and J. L. Volakis, “High-Strength, Metalized Fibers for Conformal Load Bearing Antenna Applications,” *IEEE Trans. Antennas Propag.*, vol. 59, no. 9, p. 3458, Sep. 2011, doi: 10.1109/TAP.2011.2161442.
- [44] J. P. Dunsmore, *Handbook of Microwave Component Measurements: with Advanced VNA Techniques*, ch. 5., Hoboken, NJ, USA: J. Wiley & Sons, 2012.
- [45] A. Wien, *EMPIRE XPU Manual*, Version 9.0.0, IMST GmbH, Kamp-Lintfort, Germany, Mar. 2024, [Online]. Available: <http://empire.de/documentation/manual-and-release-notes.html> (accessed on 6 Mar. 2025).
- [46] C. A. Balanis, *Antenna Theory: Analysis and Design*, 4th ed., ch. 4 and 9, Hoboken, NJ, USA: J. Wiley & Sons, 2016.
- [47] W. L. Stutzman and G. A. Thiele, *Antenna Theory and Design*, 3rd ed., ch. 3, Hoboken, NJ, USA: J. Wiley & Sons, 2012.
- [48] S. J. Orfanidis, *Electromagnetic Waves and Antennas*, ch. 2, Rutgers University, 2016, [Online]. Available: <https://ece.rutgers.edu/orfanidis> (accessed on 6 Mar. 2025).
- [49] N. Ida, *Engineering Electromagnetics*, 3rd ed., ch. 12, Heidelberg, Germany: Springer, 2015.

- [50] W. H. Hayt Jr. and J. A. Buck, *Engineering Electromagnetics*, 9th ed., ch. 11, New York, NY, USA: McGraw-Hill Education, 2018.
- [51] K. C. Yaw, *Measurement of Dielectric Material Properties*, Application Note, 2012.



VARVARA MOUZI is a biomedical engineer specializing in the development of advanced medical technologies. She holds an MSc in Translational Engineering in Health and Medicine from the National Technical University of Athens and a BSc in Materials Science and Engineering from the University of Crete. Her academic work focuses on wireless power transfer in implantable medical devices and energy-harvesting metamaterials. She has experience in R&D environments, including computational modeling, 3D printing, and ISO-standard antibacterial testing.



NEKTARIOS MORAITIS (Senior Member, IEEE) received the Diploma, and the Ph.D. degrees, all in electrical and computer engineering, from the National Technical University of Athens, Greece, in 1998, and 2005, respectively.

In 1997 he joined the Mobile Radiocommunications Laboratory of National Technical University of Athens. In 2007 he became a permanent staff as a laboratory engineer in Mobile Radiocommunications Laboratory of National Technical University of Athens. In 2014 he became a teaching and research associate (faculty staff), School of Electrical and Computer Engineering, National Technical University of Athens. He has involved in many research projects, including channel measurements, modeling, and characterization for wireless communication systems, microwave systems design, and mobile satellite communication systems. He has also participated in European projects such as ERMIS, SatNEx I and II as well as in COST 273, 259, 2100 and IC0802 activities. He has more than 90 publications in international journals, conference proceedings, and book chapters. His current research interests include millimeter wave propagation for next generation wireless communications systems, channel measurements, characterization, simulation and modeling for fixed and mobile communications systems, MIMO technology for mobile satellite systems, and biological effects of electromagnetic radiation. He is ranked in top 200 reviewers (May'21–Apr.'22 and May'23–Apr.'24), of the journal *IEEE Transactions on Antennas and Propagation*.

Dr. Moraitis is a Senior Member of IEEE, and serves as the chair of IEEE Vehicular Technology/Aerospace and Electronic Systems Joint Chapter, Greek Section since 2020.



CONSTANTINE KAKOYIANNIS (Member, IEEE) was born in Athens, Greece, in June 1977. He studied electrical & computer engineering, majoring in wireless communications, at the National Technical University of Athens, Greece, and received the Diploma (5-year degree) in 2000. In 2011, he earned from NTUA the Doctor of Engineering degree in the field of energy-efficient, wideband, compact, single-/multi-element antennas.

From 2001 to 2011, he worked as a MW/RF Antenna Engineer at the Institute of Communication & Computer Systems, NTUA (ICCS/NTUA). From 2012 to 2015 he was a Post-doctoral Research Fellow with the National Centre for Scientific Research "Demokritos", Athens, Greece, working on reconfigurable magneto-dielectric antennas. During the same period, he worked for Computer Simulation Technology (CST) AG, Darmstadt, Germany, providing technical support, training, and technical marketing services. He rejoined ICCS/NTUA in 2014–2015, where he assumed the role of Lead Antenna Engineer to research active microwave imaging antennas. Since 2016, he has been an Antenna R&D Engineer with the Antennas & EM Modeling Dept, IMST GmbH, Kamp-Lintfort, Germany, where he develops novel antenna systems from VHF up to mm-wave frequencies. He has authored over 50 papers in peer-reviewed journals and conferences, and one book chapter. He holds two patents. His research interests include small antenna theory & design, antenna miniaturization, antenna efficiency measurements, electronically scanned arrays, mutual coupling suppression, magneto-dielectric antennas, circularly polarized antennas and time-domain full-wave modeling.

Dr. Kakoyiannis is a member of the European Microwave Association (EuMA) and the European Association on Antennas and Propagation (Eu-rAAP). He received the Best Paper Award at the 2009 Int'l Conference on Sensor Technologies and Applications (SENSORCOMM'09). He was the recipient of the 2017 Int'l Workshop on Antenna Technology (iWAT 2017) Best Poster Award. He served as a TPC member on several editions of the EuCAP, LAPC, iWAT, and ASPACE conferences. He is an active reviewer for a number of IEEE Transactions, Letters, and Magazines.



KONSTANTINA S. NIKITA (Fellow, IEEE) received the diploma in Electrical Engineering and the Ph.D. degree from the National Technical University of Athens (NTUA), as well as the M.D. degree from the Medical School, University of Athens. She is a full professor at NTUA, the Irene McCulloch Distinguished Adjunct Professor of Biomedical Engineering and Medicine, at Keck School of Medicine and Viterbi School of Engineering, University of Southern California, and a 2022/2023 Global Chair at the University of Bath. She is the director of the Mobile Radiocommunications Laboratory and founder and director of the Biomedical Simulations and Imaging Laboratory at NTUA. Her current research interests include mobile health, computational bioelectromagnetics, biomedical signal and image processing and analysis, simulation of physiological and biological systems, and biomedical data science. Her published work consists of twelve books, more than 200 papers in refereed international journals, 48 chapters in books, over 400 papers in international conference proceedings, and three patents. She has been the technical manager of numerous European and National R&D projects.

Dr. Nikita is the Editor-in-Chief of the *IEEE Transactions on Antennas and Propagation* and Founding Editor-in-Chief of the *IEEE Journal of Antennas and Propagation*. She has served as chair of the LS7 Consolidator Grant Panel of the European Research Council (ERC), for granting investigator-driven frontier research in the domain of life sciences. She is a Fellow of the Institute of Electrical and Electronics Engineers (IEEE), the American Institute of Medical and Biological Engineering (AIMBE), and the European Association of Medical and Biological Engineering and Science (EAMBES). She has received various honors/awards, with the Bodossakis Foundation Academic Prize being one of them.



CONSTANTINOS VALAGIANNPOULOS (Senior Member, IEEE) was born in Athens, Greece, in 1982. Between 2015 and 2023, he was a Faculty Member of the Department of Physics at Nazarbayev University (NU), Kazakhstan, until he got unanimously elected Assistant Professor at the School of Electrical and Computer Engineering of National Technical University of Athens (NTUA), Greece.

He leads the Metamaterials Modeling and Design Group performing research on the forward and inverse design of photonic devices manipulating the light as well as on the translation of electromagnetic concepts into quantum systems. He has authored or coauthored more than 140 works published at international refereed scientific journals and presented numerous reports in scientific conferences. He has participated as Principal Investigator (PI) or co-PI in the successful execution of national and international research grants with total budget surpassing 4M USD.

Between 2010 and 2014, he was a Postdoctoral Researcher in the Group of Theoretical and Applied Electromagnetics of Complex Media at the Department of Electronics and Nanoengineering of Aalto University, Finland (advisor: Sergei Tretyakov). He has spent the academic year 2014-2015 with the Laboratory of Metamaterials and Plasmonics at the Department of

Electrical and Computer Engineering, University of Texas at Austin, TX, USA (advisor: Andrea Alù). During 2016, he was a visiting scholar at the Department of Physics of Harvard University, MA, USA (group of Efthimos Kaxiras) while in 2017 he has been a visiting Assistant Professor at the School of Physics and Astronomy, University of Southampton, UK (group of Pavlos Lagoudakis). Finally, he holds a Dipl. Eng. (Hons.) degree in Electrical Engineering from NTUA in 2004, and a Ph.D. degree on Electromagnetic Theory in 2009 from the same Institute.

Dr. Valagiannopoulos received the inaugural 2015 JOPT Research Excellence Award for his work: "Perfect absorption in graphene multilayers" and is a Senior Member of International Union of Radio Science (URSI) and OPTICA. He also received the International Dimitri Chorafas Foundation Prize for the Best Doctoral Thesis in 2008, the NTUA Thomaides PhD Thesis Award 2008, and the Academy of Finland Postdoctoral Grant for 2012-2015. He is named American Physical Society (APS) Outstanding Referee, he has won a Newton Al-Farabi Researcher Links Travel Grant for 2017, and has been the winner of the 2020 NU Teaching Award for Integrating Research and Teaching.

...